Journal of Power Sources 576 (2023) 233189

Contents lists available at ScienceDirect

Journal of Power Sources

journal homepage: www.elsevier.com/locate/jpowsour

Ultrasonic guided waves as an indicator for the state-of-charge of Li-ion batteries

Benjamin Reichmann, Zahra Sharif-Khodaei *

Department of Aeronautics, Imperial College London, London SW7 2AZ, United Kingdom

HIGHLIGHTS

- Chirp signals enable transfer of ultrasound-based battery monitoring method to any cell.
- Piezoelectric transducers validate technique on 12.5 Ah battery pouch cells.
- Dominant frequency in response to tone burst signal indicates state-of-charge.

ARTICLE INFO

Keywords:
Lithium-ion battery
Ultrasonic guided waves
Dominant frequency
State-of-charge
State-of-health
Temperature correction

ABSTRACT

Conventional battery management systems rely on cell voltage, current, and temperature to predict the battery state-of-charge and state-of-health, but their accuracy is limited. To overcome this limitation, ultrasonic probing has been proposed as a novel battery monitoring technique. This paper introduces the use of ultrasonic chirp signals for the transfer of ultrasound-based battery monitoring techniques without requiring prior knowledge of the architecture of the cell. To validate this technique, small, lightweight piezoelectric disc transducers that can be easily installed on off-the-shelf battery pouch cells were utilized for large cells with a capacity of 12.5 Ah. Furthermore, the dominant frequency of the response signal to a Hanning-windowed tone burst signal was identified as a quantitative state-of-charge indicator. A predictive model was developed to compare the performance of this indicator with that of previous ultrasound-based state-of-charge prediction methods. The influence of the cell temperature and cycle age on ultrasonic guided wave propagation was also investigated and isolated for analysis.

1. Introduction

The climate crisis urges the entire transport industry to find energy storage systems that do not require fossil fuels and the market share of battery-powered cars increases rapidly [1]. A major challenge in the path to the certification of electrically powered vehicles, especially aircraft, is the design of reliable and safe battery systems. Certain failure conditions for Lithium-ion (Li-ion) batteries can lead to violent battery fires and explosions. In land-based vehicles, passengers can evacuate within a few seconds. In contrast, air transport vehicles must operate safely for an extended period after the occurrence of a battery malfunction without endangering the health of the passengers or the integrity of the airframe. Therefore, advanced monitoring techniques for battery cells are required to prevent battery fires in the first place.

Conventional battery management systems (BMS) typically use open-circuit voltage, current integral, and temperature data to estimate the state-of-charge (SoC) and state-of-health (SoH). Advanced predictions methods have been introduced including combined short-term, long-term memory neural networks to predict the SoC and SoH accurately based on these parameters [2–4]. Even though the prediction techniques are mature, they still rely on the external parameters of the cell. Unfortunately, the open-circuit voltage can only be measured when no electric load is applied to the cell, and hence, not during operation. Coulomb counting must be performed continuously and cannot account for internal losses in the cell. However, a Li-ion battery can be analysed not only as an electrochemical system but also as a layered multi-material composite. Because energy is stored by relocating Li ions between the cathode and the anode of the cell, the compositions of both materials change with the SoC. This fact can be utilized in ultrasonic testing. Ultrasonic guided waves have been used extensively in detecting damage in metallic and composite structures from small coupons to large structures [5–7]. Their propagation in a medium is dependent on multiple factors including the density, modulus, and

* Corresponding author.
E-mail addresses: benjamin.reichmann21@imperial.ac.uk (B. Reichmann), z.sharif-khodaei@imperial.ac.uk (Z. Sharif-Khodaei).
URL: https://www.imperial.ac.uk/people/z.sharif-khodaei (Z. Sharif-Khodaei).

https://doi.org/10.1016/j.jpowsour.2023.233189
Received 17 February 2023; Received in revised form 3 May 2023; Accepted 10 May 2023
Available online 24 May 2023

porosity [8] of the structure. In the active materials of a Li-ion battery cell, these properties are dependent on the SoC, as well as on the temperature and cycle age. Consequently, ultrasonic guided waves can be used to monitor the SoC of Li-ion batteries [8–10]. In contrast to traditional imaging techniques based on electrons, ions, neutrons, or X-ray radiation, ultrasonic guided waves provide rich information about the physical properties of a sample without damaging it or requiring its disassembly [11].

Initial work using ultrasonic transducers on Li-ion cells was performed by Sood et al. in 2013 [12]. The authors intended to monitor the interfaces between the active materials of the anode and cathode and their respective current collector foils. Using two 1/4″ (6.35 mm) diameter transducers centrally on the upper and lower sides of a pouch cell with a frequency of 5 MHz and signal strength of 400 V, they analysed the reflected and transmitted parts of the signal, respectively. The authors found that the transmitted signal was much weaker after the cell was cycled, which they attributed to the degradation of the interfaces. During cycling, gases such as CO_2, CH_4, and C_2H_4 are released and form pockets at the interfaces that push away the electrolyte and therefore decouple sections of the cell, leading to a reduction in capacity [12]. In 2015, Hsieh et al. [9] used a similar setup with two 2.25 MHz transducers on different cell types, including $LiCoO_2$ pouch cells, to demonstrate the global trend of decreasing time-of-flight (ToF) and increasing signal amplitude (SA) when the SoC increases. In addition to this global trend, they found exemptions close to the end of discharge, where $LiCoO_2$ approaches a hexagonal-to-monoclinic phase transition that can quickly change the density and Young's modulus of the cathode [9]. When the cell is recharged, this phase shift is reversed, and the signal intensity drops again [9]. Furthermore, Hsieh et al. found a slight decrease in the signal intensity close to 100% SoC, which is related to a two-phase staging reaction.

Gold et al. [8] introduced the use of small piezoelectric disc transducers on Li-ion battery cells in 2017. Similar to the studies above, they probed their 1.2 Ah pouch cell along the thickness dimension with two sensors mounted on opposite sides of the cell. In their study, they found that the amplitude of the second peak in the response signal increased with increasing SoC, whereas the time-of-flight decreased. The data collected during charging in steps of 20% SoC were approximated as linear trend. During discharging, Gold et al. observed a hysteresis effect in the SA. In 2018, Ladpli et al. [10] used ultrasonic disc transducers in a pitch-catch mode along the surface of a 3.65 Ah graphite/NMC Li-ion pouch cell. Throughout the cycling with low currents of $C/10$, ultrasonic guided waves were introduced into the cell using five-cycle tone burst signals with a centre frequency of 125 kHz. In agreement with Gold et al. [8], a decrease in the ToF and an increase in the SA were observed during charging. For similar SoCs, higher signal amplitudes were observed during charging than during discharging. Towards 0% and 100% SoC deviations from the global trend were detected for the signal amplitudes which had been found by Hsieh et al. [9] too. The setup introduced by Gold et al. and further developed by Ladpli et al. can be deployed in field operations and is also used in this study. However, the ultrasonic signal used for probing a cell must be adjusted to the geometry and material properties of the cell. The representative computational models often used for this purpose require detailed knowledge of electrode stacking as well as the dimensions and material properties of the constituents [8,10]. Because this information is often protected as an intellectual property of the cell manufacturer, an alternative method is sought to adjust the ultrasonic signal to the cell at hand. Therefore, chirp signals comprising a wide range of excitation frequencies are introduced in this study to easily adjust the ultrasonic input signal to any cell (Section 3.1). In this report, through chirp signals, the ultrasonic SoC indication is adjusted to cells with a nominal capacity of 12.5 Ah (size for use in electric vehicles), whereas most published studies (e.g., [8,10,13–15]) employed small cells used for smartphones or other personal electronics.

Additionally, the dominant frequencies in the responses to Hanning-windowed tone burst signals are considered as an indicator of SoC. Recently, Liu et al. [15] published the results of guided wave analysis of a 4.3 Ah Li-ion pouch cell. In addition to the features in the time domain, Liu et al. [15] observed a shift and amplitude change in the frequency domain when the SoC was changed. However, the authors were only able to show qualitative changes in the dominant frequency owing to limitations in frequency resolution. In this study, the frequency response is analysed using a significantly larger number of discrete Fourier transfer points, and the shift of the dominant frequencies is identified to correlate quantitatively with the SoC (Section 3.3). Eventually, the dominant frequency of the response to a Hanning-windowed tone burst signal is compared to the established indicators ToF and SA through a prediction algorithm for the SoC introduced in Section 3.6.

All ultrasound-based battery monitoring indicators detect changes in the modulus and density of the cell structure [16]. Because both are influenced by the temperature and cycle age of the cell [17], Sections 3.4 and 3.5 are dedicated to identifying and isolating these factors.

2. Experimental set-up and methods

2.1. Set-up for charging and discharging

WS-NCM12.5 Ah cells with an NMC cathode were supplied by Lithium System GmbH, Am Dorfbach 36, CH-8307 Illnau, Switzerland. The operating voltage range of the cell is 3.0 to 4.2 V. For electrochemical cycling, a BioLogic VSP-3e potentiostat with a booster FlexP0060 was used. To satisfy the operational limits of the cell, discharging currents up to $I_{Limit-} = 2C = 25$ A and charging currents up to $I_{Limit+} = 0.5C = 6.25$ A were used. At a rate of $1C$, the current is set such that the nominal capacity of the cell would be transferred within one hour. Hence, for a cell with a nominal capacity of 12.5 Ah, $1C = 12.5$ A. If the cell is charged at a higher C-rate, for example, $2C = 25$ A, the charging time is reduced. In the subsequent descriptions, the following conventions are applied: When the discharge current is lower than the maximum allowable charging current of $0.5C = 6.25$ A, the same current was used for discharging and charging. E.g., for a '$0.2C$-cycle', both the charging and discharging currents were selected to be 2.5 A. If the peak discharge current was above the charging limit, the charging was conducted at $0.5C$. Hence, a '$2C$'-cycle refers to a discharge current of 25 A and charging current of 6.25 A. Throughout this report, C-Rates are provided as a fraction of the nominal cell capacity of $C_{nominal} = 12.5$ Ah, even though a slightly higher capacity of $C_{real} \approx 13.4$ Ah was measured. The potentiostat was controlled using EC-Lab software, which was also used to collect electrical parameters throughout the experiments, including voltage, current, and charge. Furthermore, the cell temperature was monitored and recorded using a type-K thermocouple connected to the potentiostat. Data from the potentiostat were recorded at time steps of 1 s.

A constant-current-constant-voltage (CCCV) protocol was selected for charging and discharging operations. The charging/discharging process was ended when the amplitude of the current dropped below $I_{threshold} = 1/20C = 0.625$ A. Between any charging and discharging sequences, the cell was left to relax for 30 min.

The SoC was calculated based on the charge drawn from and supplied to the cell. The difference in charge Q to the chosen reference Q_{min} at the end of discharge was computed and divided by the charge range $Q_{max} - Q_{min}$ of the respective cycle, according to formula (1).

$$SoC = \frac{Q - Q_{min}}{Q_{max} - Q_{min}} \tag{1}$$

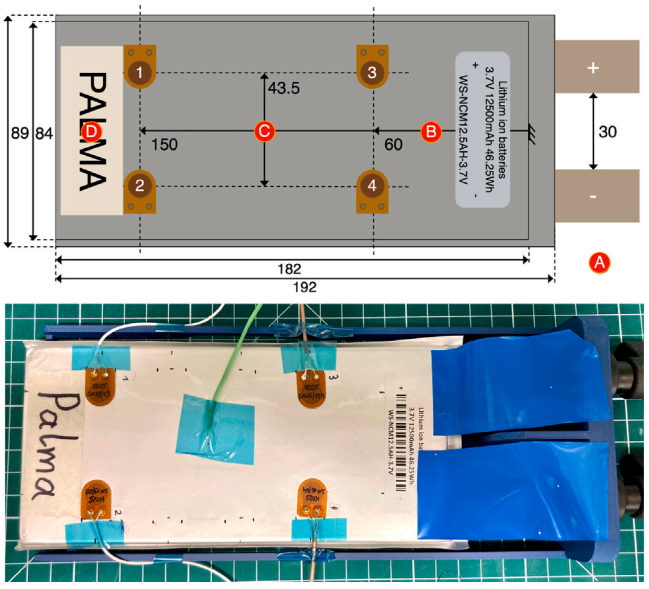

Fig. 1. Top: Schematic of cell WS-NCM12.5AH-3.7 including piezoelectric transducer discs (brown) and thermocouples (red), Bottom: Picture of cell WS-NCM12.5AH-3.7 including piezoelectric transducer discs and one thermocouple.

2.2. Set-up for ultrasonic guided wave probing

To monitor the changing mechanical properties of the cell, ultrasonic guided waves were actuated and sensed through permanently surface-mounted piezoelectric disc transducers of the type PI P-876K025. The setup was inspired by work conducted by Ladpli et al.. Compared with conventional ultrasonic probes, such as those used by Hsieh et al. and Robinson et al., surface-mounted disc transducers can be integrated in batteries for consumer electronics or in battery packs for electric vehicles because of their small size and weight. As they are permanently attached, errors in the transducer distance or variations in the attachment pressure can be avoided. Four sensors were attached to the same side of the cell, as shown in Fig. 1 and the data recorded on Path 1–2 were used in this study.

An attempt was made to mount the piezoelectric disc transducers using double-sided tape 'Advance Tapes AT395' to allow repositioning of the transducers. However, a trial on an aluminium plate showed that the signal amplitude and modal clearness were severely compromised. Therefore, 'Loctite Super Glue All Plastics, 2G' was used to attach the sensors to the battery cell.

The sensors were operated in pitch-catch mode, where one transducer acted as an actuator and the remaining transducers were receivers. A software initially developed by Lambinet and Sharif Khodaei [18] and enhanced by Rodrigues in the Structural Integrity and Health Monitoring Group at Imperial College London [19] was used to create the actuation signal and operate the waveform generator 'NI PXI-5412' and oscilloscope 'NI PXI-5105'. The input signal data had a sampling frequency of 100 MHz, and the response signals were recorded with a sampling frequency of 60 MHz. During the charging–discharging cycles, guided wave measurements were conducted every 2 to 6 min depending on the charging and discharging speed, to collect a sufficient number of data points throughout the entire cycle. The data recorded by the potentiostat (voltage, current, charge, temperature, etc.) were synchronized with the guided wave measurements using the absolute timestamp saved to each data point. Because the time step for the potentiostat measurements was as small as 1 s, two adjacent data points were always available for each guided wave measurement with a distance of less than 1 s. When synchronizing the data, each guided wave measurement got a value for the corresponding voltage, current, cell temperature, etc., assigned using the weighted average of the two adjacent data points from the potentiostat. For example, if a guided wave measurement is taken at time T_{GW} = '12:55:05' and the potentiostat records the voltages U_1 = 4.12 V at T_1 = '12:55:04.419' and voltage U_2 = 4.11 V at T_2 = '12:55:05.419', the voltage assigned to this particular guided wave measurement is calculated as shown in formula (2).

$$U_{GW} = \begin{bmatrix} U_1 & U_2 \end{bmatrix} \begin{bmatrix} 1-|T_1-T_{GW}| \\ 1-|T_2-T_{GW}| \end{bmatrix} \approx 4.114V \tag{2}$$

3. Results and discussion

3.1. Optimization of tone burst signal using chirp

Ultrasonic guided wave measurements which have been introduced as battery monitoring technique [8,10] are originating from structural health monitoring techniques. For the later, piezoelectric disc transducers have been used to detect damage in structural components. Typically Hanning-windowed tone burst signals are deployed since they allow the excitation of the structure with only a small frequency band centred around one frequency (e.g. [20]). This leads to limited wave modes in the probed structure. Therefore, specific wave packages can be detected and identified more easily. The centre frequency can be adjusted such that specific wave modes are excited and the propagation speed of the wave is within the nondispersive frequency band. In this zone, the propagation speed does not change significantly if the frequency is altered by the interaction with damage [16]. Ladpli et al. (2018) used five-cycle Hanning-windowed tone burst signals with centre frequencies between 100 and 200 kHz to excite their battery cell [10].

To identify a suitable frequency, either different frequencies can be tested until the response signal shows clear wave packets or the interaction between the ultrasonic guided wave and the structure needs to be analytically or numerically estimated to compute the wave modes produced by a specific input frequency. Multiple authors, including Hsieh et al., Gold et al., Ladpli et al., have developed advanced models to simulate the propagation of ultrasonic waves in battery pouch cells. However, these models require knowledge of the internal structure of the cells, including the stacking sequence, number and thickness of layers, and material properties of the constituents *a priori*. The complexity of the computational model is further increased by the interaction of waves with the liquid electrolyte contained in the cell. If SoC monitoring shall be applied to different cell types without the need for a detailed computational model, another method of adjusting the signal to the cell is required. To this end, a chirp signal is used in this study, as suggested by Michaels et al. [21] and utilized in [7,22] for structural health-monitoring purposes.

A chirp signal is a finite signal that sweeps over a range of frequencies. If the response to a chirp signal is recorded for a structure, then the response to any tone burst signal within the frequency range of the chirp signal can be reconstructed [21]. The chirp signal can be expressed by Eq. (3) where f_0 is the initial frequency, B is the bandwidth, and T is the chirp duration [21]. The corresponding Fourier transform is denoted by $S_c(\omega)$. Both are illustrated in Fig. 2(a) and (b), respectively.

$$s_c = w(t)sin(2\pi f_0 t + \frac{\pi B t^2}{T}) \tag{3}$$

$$R_t(\omega) = R_c(\omega)\frac{S_t(\omega)}{S_c(\omega)} \tag{4}$$

The signal excited by one of the piezoelectric transducers propagates through the battery cell and undergoes change. This alteration can be expressed as transfer function $H(\omega)$ in the frequency domain. If the structure can be represented as a linear system [21], the response to an input function $S(\omega)$ can be computed as $R(\omega) = H(\omega)S(\omega)$ where $H(\omega)$ is the transfer function of the cell with instrumentation that is valid

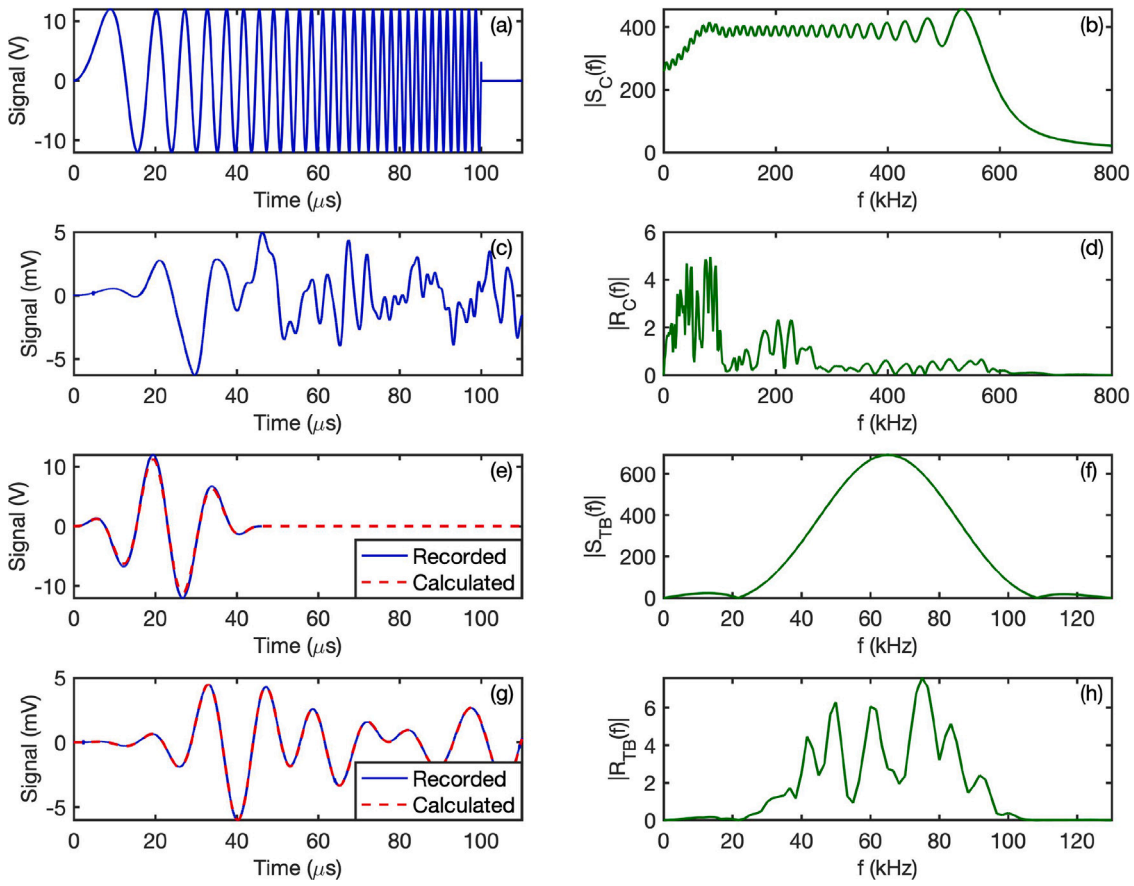

Fig. 2. Chirp reconstruction at 100% SoC for path 1-2: (a) Chirp signal with frequency range of 1–600 kHz in time domain (b) Frequency content of chirp signal (c) Response to chirp signal in time domain (d) Frequency content of response to chirp signal (e) Recorded (blue) and calculated (dashed red) three-peak tone burst signal with centre frequency 65 kHz in time domain (f) Frequency content of recorded tone burst signal (g) Recorded (blue) and calculated (dashed red) response to tone burst signal in time domain (h) Frequency content of calculated response to tone burst signal. (For interpretation of the references to colour in this figure legend, the reader is referred to the web version of this article.)

for both the chirp signal and tone burst signal within the frequency range of the chirp signal [21]. Hence, once the response $R_c(\omega)$ to a chirp signal $S_c(\omega)$ covering the frequency range of the desired tone burst signal is recorded, the expected response $R_t(\omega)$ in the frequency domain to any tone burst signal $S_t(\omega)$ within the bandwidth of the chirp signal can be calculated using Eq. (4).

Therefore, the following method is suggested to adjust the ultrasonic guided wave signal to any cell at hand. First, a chirp signal with a wide frequency range is created, and the corresponding response of the structure recorded (see Fig. 2(a) and (c)). The frequency content of both the signal and the response is shown in 2(b) and (d). With this data, the response to any tone burst signal within the frequency range of the chirp signal may be computed according to Eq. (4). Next, the desired tone burst signal is created in the time domain, as shown by the red dashed line in Fig. 2(e), and the frequency content calculated using the Fast Fourier algorithm (Fig. 2(f)). The response to the tone burst signal (Fig. 2(h)) is computed according to Eq. (4) and the corresponding tone burst response in time domain obtained using the inverse Fast Fourier transformation. Fig. 2(e) and (g) show the calculated tone burst signal and the reconstructed response, respectively, using a dashed red line. For validation, the same tone burst signal was used to excite the cell, and the recorded response is plotted in blue, showing a precise fit with the reconstructed response in Fig. 2(g). This procedure allows the evaluation of the response of the cell to multiple tone burst signals without recording the response to each signal on the actual cell.

To monitor the SoC of a cell, the characteristics of the response to the tone burst signal must be correlated with the changes in the SoC. In this section, the optimization of the number of excitation cycles in the tone burst signal and its centre frequency is discussed. Fig. 3 displays the tone burst signals (a) with 5 and (b) 1.5 excitation cycles and the corresponding responses at different states of charge. For the response signals the colour is changed from light to dark blue incrementally to illustrate the SoC variation from 0% to 100% SoC. The black line shows the scaled excitation signal to compare the possible overlap of the actuation and sensing signals, due to the short physical distance between the transducers. The dashed lines show the reconstructed response signals based on the chirp signals recorded on the cell. The solid lines indicate the magnitudes of the corresponding Hilbert envelopes and the dots on the centreline highlight the positions of the respective signal peaks. It is important to note that the frequency content of a tone burst signal becomes narrower when more cycles are included in the excitation signal. Thus, a signal with a very low number of cycles contains a wider frequency band. However, at a given centre frequency, a signal with more cycles has a longer duration. The input signals with 5 and 1.5 cycles at 65 kHz have lengths of 78 μs and 24 μs, respectively. For the signal with 5 cycles, (a), the input signal duration is significantly longer than the ToF for the first peak. In contrast, the input signal with only 1.5 cycles, (b) ends just after the signal arrives at the second transducer. If multiple wave modes are excited, a long signal duration can lead to interference of the wave modes.

In all the response signals, more than one peak is evident, with the first peak having a higher amplitude than the second. For a signal with 5 cycles, two distinct wave packages can be identified at 100% SoC (dark blue). However, at lower charge states, the second peak fades in amplitude to a point where the minimum between the first peak and second peak is barely identifiable. For the signal with 1.5 cycles, the

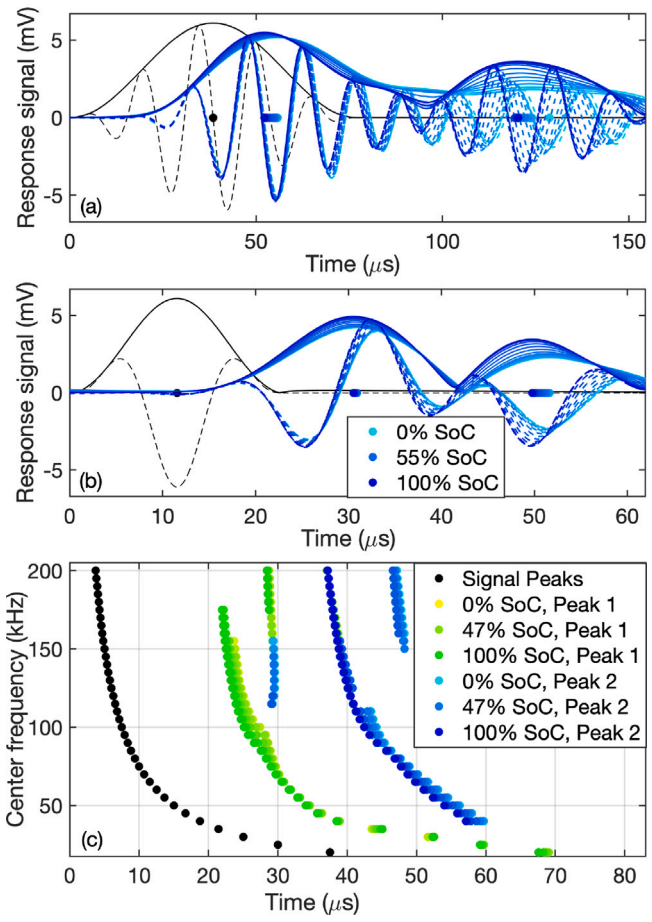

Fig. 3. Tone bursts for path 1–2 recorded during charging at $I = 6.25$ A on 07.07.2022 with a temperature variation of $\Delta T = 2.21$ K: (a) centre frequency 65 kHz with 5 cycles; (b) centre frequency 65 kHz with 1.5 cycles; (c) various centre frequencies with 1.5 cycles showing only the peak positions. (For interpretation of the references to colour in this figure legend, the reader is referred to the web version of this article.)

magnitude of the response Hilbert envelope reaches almost 0 V between the first and the second peak, making both peaks clearly identifiable at all states of charge. Therefore, signals with 1.5 cycles were chosen for the following experiments.

In addition, the different characteristics of the first and second peak in the respective response signals can be compared based on Fig. 3(a) and (b). The first peak is stronger in amplitude; however, this is not the most relevant criterion for the analysis. Rather, features that show a significant change with SoC are sought. A larger variation in the ToF and SA in absolute numbers improves the signal-to-noise ratio. The second peak shows a much wider variation in ToF and SA than the first peak and is therefore chosen for subsequent analyses. Further peaks (after the second) are not considered, as the wave packages become less distinct, which could be caused by interactions with the cell boundaries (compare Fig. 1).

The same technique can be used to probe different centre frequencies. Once the chirp signal response has been recorded for different SoCs, responses to tone burst signals with different frequencies can be computed automatically, and only the relevant output parameters are plotted. For example, the peaks of the response signals can be plotted for each frequency in the relevant range to visualize the spacing of the ToF over the SoC range. A wider spacing allows for an improved signal-to-noise ratio as the absolute differences increase. The same procedure may be applied to any desired parameter (ToF, SA, or dominant frequency). For the cell WS-NCM12.5 Ah, an example of such a plot is shown in Fig. 3(c) for the position of the response peaks at different centre frequencies of tone burst signals with 1.5 cycles. The first and second peak appear consistently and have similar distances from each other for frequencies between 40 kHz and 110 kHz. At 110 kHz, the first peak is at approximately 25 μs and the second peak is at approximately 42 μs. At 120 kHz, another peak at approximately 29 μs becomes stronger than the peak at 42 μs for low states of charge. For low frequencies of up to 80 kHz, the second peak shows a larger spread at the time of arrival than the first peak. Based on the criteria discussed above, a tone burst signal with 1.5 cycles and a centre frequency of 65 kHz was selected as the optimum waveform to excite the WS-NCM12.5 Ah cell.

Using the procedure outlined in this section, the ultrasonic signal may be easily adjusted to any cell at hand. Instead of probing different tone burst signals at each SoC, only a chirp signal needs to be recorded throughout one charge–discharge cycle. The identification of the most suitable tone burst signal can be performed during post-processing.

Subsequently, the suggested method was applied to a WS-NCM12.5 Ah cell. First, the indicators time-of-fight (ToF) and signal amplitude (SA) are briefly analysed to validate the method in Section 3.2. Next, the dominant frequency of the response to a tone burst signal is investigated as a novel state-of-charge indicator in Section 3.3.

3.2. Validation of time-of-flight and signal amplitude as state-of-charge indicators

To validate the method for the established indicators ToF and SA [10], the responses of the battery cell to tone burst signals were reconstructed from chirp signals with a frequency range of $1-600$ kHz which were recorded over the duration of a discharge–charge cycle at a current of $I = 0.34C = 4.25$ A. The results are shown in Fig. 4. Similar to the trends found by Ladpli et al. [10], a decrease in SoC correlates to an increase in the ToF in plot (a), and vice versa. Interestingly, this trend is not symmetric. The SA in plot (b) decreases when the SoC decreases. Both the ToF and SA show larger gradients at the start of discharging and towards the end of charging. Hence, they are more sensitive at 20%–100% SoC. In agreement with the results of Hsieh et al. (2015) [9] and Ladpli et al. (2018) [10], a deviation of the trend can be observed towards the end of discharge. Hsieh et al. attributed this to a phase transition of the cathode which could have a major impact on its density and young's modulus. In accordance with the cell datasheet, plot (c) shows a small initial drop of the cell voltage, followed by a piecewise linear decline with decreasing SoC. The cell temperature shown in plot (d) has a low overall variation of $\Delta T = 2.73$ °C, owing to the low charge/discharge current. The temperature increases during discharging, with the peak located at the end of discharge. It decreases during the 30 min rest period and increases slightly again during charging. While Ladpli et al. [10] conducted their experiment at a very low current and corresponding constant temperature, the declining temperature during the rest period seems to impact the ToF and SA in this work, as suggested by [14]. Further analysis of the impact of temperature is presented in Section 3.4.

Furthermore, it can be concluded that the ultrasonic indicators ToF and SA complement the cell voltage well for SoC monitoring purposes. While the guided wave features show a high susceptibility to changes in SoC between 100% and 20% SoC, their gradient is small between 20% and 0% SoC. On the other hand, for the cell voltage, the largest changes are found at low charge states.

3.3. Demonstration of dominant frequency as state-of-charge indicator

With the results in Section 3.2, the experimental set-up and data processing is validated against the results of previous research including [8–10] using the ToF and SA. Both are characteristics of the response signal in the time domain. Liu et al. [15] set out to analyse the dominant frequency in the response to a tone burst signal. Due

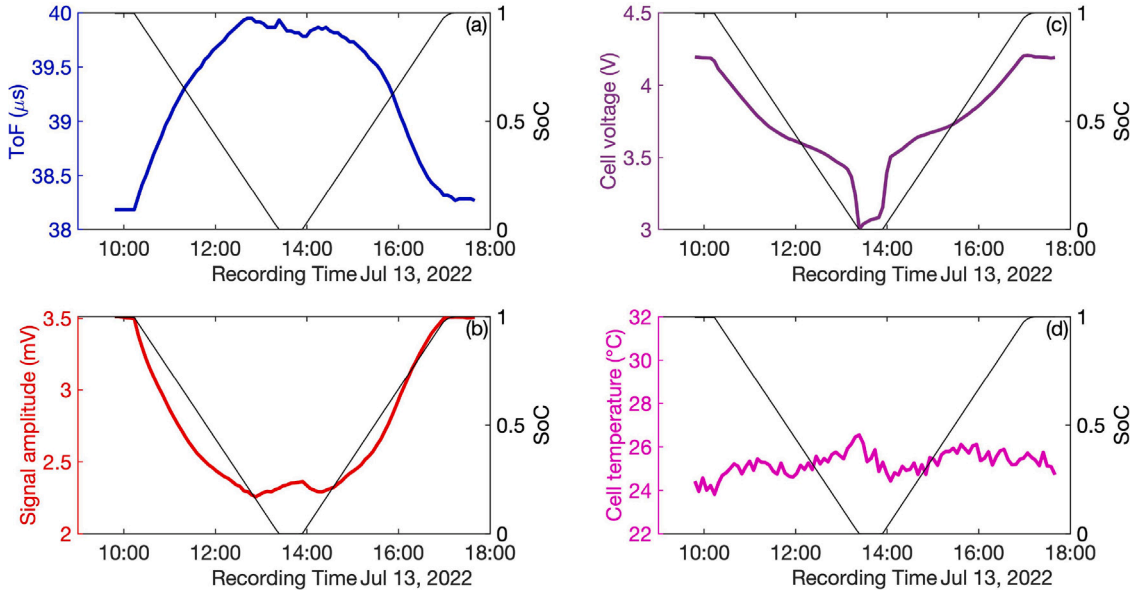

Fig. 4. (a) ToF of the second response peak, (b) SA of the second response peak, (c) cell voltage, (d) cell temperature and SoC (in all plots) during a discharge–charge cycle at $I = 0.34C$ using a tone burst signal with 1.5 cycles and a centre frequency of 65 kHz on path 1–2 recorded on 13.07.2022 with a temperature variation of $\Delta T = 2.73$ K.

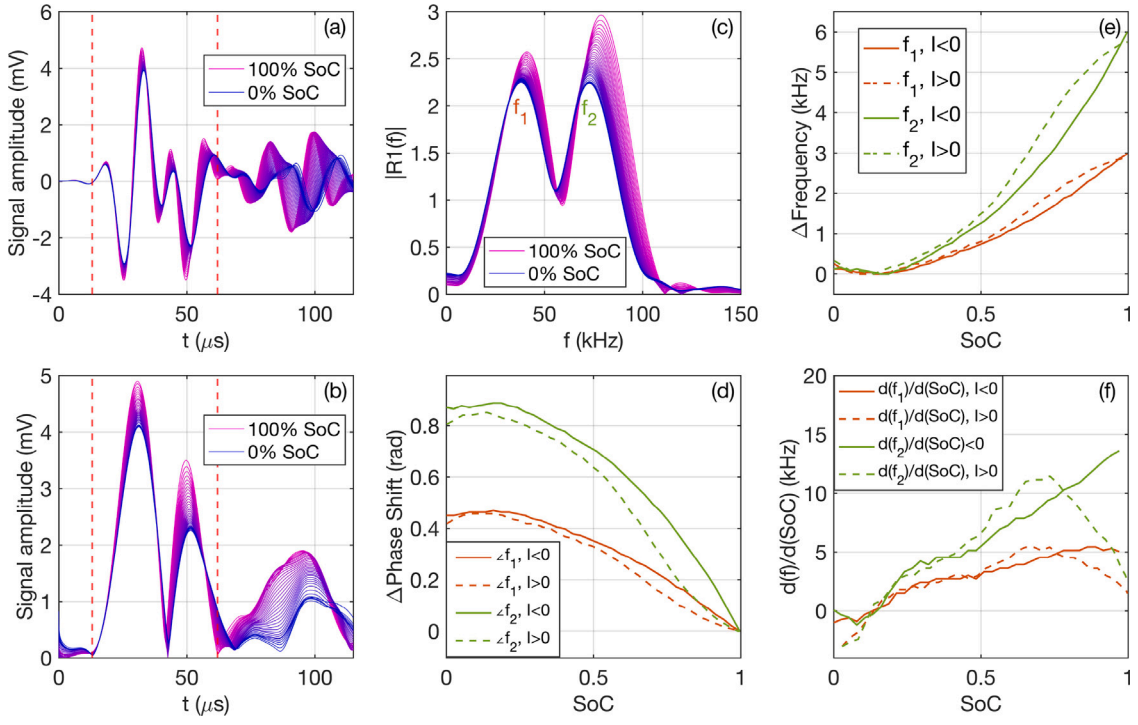

Fig. 5. (a) Response signal in time domain and (b) corresponding Hilbert envelope for different SoC during discharge with $I = 0.34C$ using a tone burst signal with 1.5 cycles and a centre frequency of 65 kHz on path 1–2 recorded on 13.07.2022 with a temperature variation of $\Delta T = 2.73$ K. (c) Frequency content of first two wave packets. (d) Variation of phase angle of the dominant frequencies identified in (c). (e) Variation in dominant frequencies with SoC (f) Moving average of gradient d(f)/d(SoC) with window size 5.

to the low fidelity analysis of the frequency content, they could only show qualitative correlations between the dominant frequency of the response to a tone burst signal and the SoC. This work aims to provide a sufficiently fine frequency resolution to utilize the dominant frequency of the response to a tone burst signal as an additional SoC indicator to supplement the indicators in time domain.

Examining Fig. 3(b) again, it is noticed that not only the peaks, but the entire second wave packet is shifted. It is apparent that the phase shift of the signal increases with time, suggesting a change in the dominant frequency. The frequency appears higher (shorter period) towards 100% SoC. A similar observation was made by Liu et al. [15] for some states of charge. These observations are substantiated in Fig. 5. Based on chirp signal responses recorded during a cycle with $I = 0.34C = 4.25$ A, the responses to a tone burst signal with 1.5 cycles and a centre frequency of 65 kHz were reconstructed and are plotted in Fig. 5(a). Plot 5(b) contains the associated Hilbert envelopes to simplify the identification of relevant wave packets. In both plots, the dashed red lines indicate the first two wave packets. The sequence enclosed by these red lines was analysed for its frequency content, and the results are shown in plot (c). It is important to note that the discrete Fourier

transform must be computed with a sufficiently fine spacing to resolve the small changes in the dominant frequencies. The frequency spacing is given by Δf in Eq. (5) where f_s is the sampling frequency (60 MHz) and $n = mk$ is the number of discrete Fourier points expressed as a multiple m of the signal length $k = \Delta t f_s$ with Δt being the duration of the analysed signal section (approx. 50 μs, Fig. 5(a)). To achieve a frequency spacing Δf of approximately 40 Hz, $m = 500$ was selected.

$$\Delta f = \frac{f_s}{n} = \frac{f_s}{m \cdot k} = \frac{f_s}{m \Delta t f_s} = \frac{1}{m \Delta t} \tag{5}$$

In [15], a frequency spacing of approximately 2500 Hz was used. Considering the dominant frequency range of approximately 6 kHz, as displayed in Fig. 5(e), no quantitative analysis would have been possible. Note that, for the reconstruction and analysis in the time domain of a tone burst response from a chirp signal, as explained in Section 3.1, a significantly lower number of discrete points (e.g. $n = 2k$) is sufficient.

In Fig. 5(c), the two dominant frequencies are identified as $f_1 \approx 38 - 41$ kHz and $f_2 \approx 73 - 79$ kHz, respectively. Plot (d) shows the phase shift of the dominant frequencies with varying SoC. It can be observed that the phase shift decreases with an increase in SoC. The magnitude of the gradient of the phase shift increases towards a high SoC. The phase shift displayed in Fig. 5(d) is likely a result of a shift in the dominant frequencies. Plot (e) illustrates a clear increase in both the dominant frequencies with increasing SoC. Near 0% SoC, the gradient of the dominant frequency $\partial(f)/\partial(SoC)$ is approximately zero. At approximately 20% SoC, the gradients of both the central frequencies start to increase. This is even more evident when plotting the gradient $\partial(f)/\partial(SoC)$ in plot (f). During discharging, both gradients are almost linear, suggesting a quadratic correlation between the dominant frequencies and SoC. However, during charging, the gradient starts to decrease again after the cell reached 70% SoC.

It is worth noting again that all the response signals used in Fig. 5 are responses to tone burst signals with a centre frequency of 65 kHz. However, plot 5(e) indicates that the central frequencies detected in the response signal varies as a function of SoC.

3.4. Temperature influence

The data analysed up to this point were recorded during charging and discharging cycles with currents no larger than $0.5C = 6.25$ A and corresponding low temperature variations of $\Delta T = 1 - 3$ °C throughout the entire cycle. For higher C-rates, larger temperature variations were observed. At $1C$, the temperature varied by $\Delta T = 5 - 5.7$ °C and for $2C$ cycles variations of $\Delta T = 7.9 - 12.3$ °C were measured. From research on damage detection using ultrasonic guided waves, a linear correlation between temperature and ToF as well as SA is known for materials such as aluminium and CFRP ([23–25]). Furthermore, a shift in the central frequency of the response signal can be linked to changes in temperature [26].

Owen et al. [14] characterized the temperature impact on their ultrasonic measurements on a 210 mAh pouch cell (PL-65168-2C, AA Portable Power Corp., U.S.A). The authors used a 6 mm diameter non-permanently mounted ultrasonic probe in pulse-echo mode to monitor the SoC and other parameters of the cell. For a temperature variation between 0 ° C and 50 °C, Owen et al. observed a linear increase in the ToF. The gradient of this trend changed slightly with the SoC of the cell. The SA was found to decrease with increasing temperature. Based on these findings, it was deemed necessary to account for the influence of temperature on the guided wave features when analysing charging–discharging cycles with larger temperature variations.

To isolate the influence of temperature on the ToF, SA, and dominant frequency, an experiment was conducted in which the cell was cooled and heated at a constant state of charge. The cell was first placed in a refrigerator at 5 °C for at least 60 min. Subsequently, three thermocouples were mounted on the cell, as indicated by the red circles in the cell schematic in Fig. 1. Thermocouple 'A' was used to monitor the ambient temperature while thermocouples 'B'-'D' indicated the cell temperature. With the thermocouples and piezoelectric transducers attached, the cell was placed in an oven and heated at approximately 45 °C for approximately one hour until the thermocouples on the cell indicated 40 °C. Once the cell temperature reached 40 °C, the oven door was opened and the cell was left to cool to room temperature. Chirp signals were recorded throughout the heating and cooling periods, and the analysed 1.5 cycle, 65 kHz tone burst signals were reconstructed, as explained in Section 3.1. The experiment was repeated at 0%, 33%, 67%, and 100% SoC. The maximum difference read between any of the three thermocouples on the cell was 0.87 °C and the average spread was only 0.31 °C. Therefore, spatial differences in the cell temperatures were not considered. Instead, the mean cell temperature was used. For the analysis, only the temperature range of 22–35 °C was considered, as only this temperature range was concerned during the discharge–charge cycles.

Table 1
Temperature and aging influence on ToF, SA and dominant frequency compared to parameter range observed during cycle with $I = 0.34C = 4.25$ A recorded on 13.07.2022.

	SoC 0-1	Temperature	Aging
ΔToF	−1770 ns	109 ns/°C 6.16%	−1.35 ns/cycle −0.08%
ΔSA	1255 μV	−35.3 μV/°C −2.81%	9.62 μV/cycle 0.77%
Δf	6000 Hz	−170 Hz/°C −2.83%	5.79 Hz/cycle 0.10%

Eight linear regression models were set up, with two separate models for each SoC, to split the data collected during heat up and cool down. For the dominant frequency, the maximum deviation of any regression slope from the average slope of $m_{Freq} = -170$ Hz/°C is 14.66%. The ToF average slope is $m_{ToF} = 0.109$ μs/°C, and the individual slopes deviate in inclination by up to 19.85%. With an average slope of $m_{SA} = -0.0353$ mV/°C and a maximum deviation of 35.18%, the prediction of the temperature influence on the SA is less certain than for the dominant frequency and ToF. To put the temperature influence on the dominant frequency into perspective, the discharge–charge cycle displayed in Figs. 4 and 5 should be considered again. When changing the SoC between 0% and 100% in the 0.34C cycle illustrated there, the second dominant frequency changes by 6000 Hz, the ToF by −1700 ns, and the SA by 1255 μV. The third column of Table 1 shows the impact of a one degree change in temperature in comparison.

The temperature correction models for the dominant frequency, ToF, and SA developed above were applied to two discharge–charge cycles recorded at different C-rates. Fig. 6 is divided into two columns. The left plots (a), (c), and (e) show the cycle recorded at $I = 0.34C = 4.25$ A, and the right plots (b), (d), and (f) represent the cycle recorded at $I = 2C = 25$ A. The specific data points are indicated with dots if I = 0, upward-facing triangles for data recorded during charging, and downward-facing triangles for points recorded during discharging.

Starting with plot (e), the originally recorded dominant frequency is shown as a dashed red line, whereas the temperature-corrected data are plotted as a solid red line. The linear correction model for the influence of temperature on the dominant frequency was applied using a reference temperature of 25 °C. A correction of −170 Hz/°C was hence used for each degree temperature difference from the reference temperature. The same procedure was applied using the respective correction models for ToF and SA in plots 6(a) and (c), respectively. Generally, it is clear from the first column plots that the temperature correction has only a minor influence on the values collected during the $0.34C$ cycle because the temperature range of the data used for these plots is only $\Delta T = 2.32$ °C.

The second column of plots (b,d,f) shows the original and temperature-corrected data for a $2C$ cycle ($2C$ discharging and $0.5C$

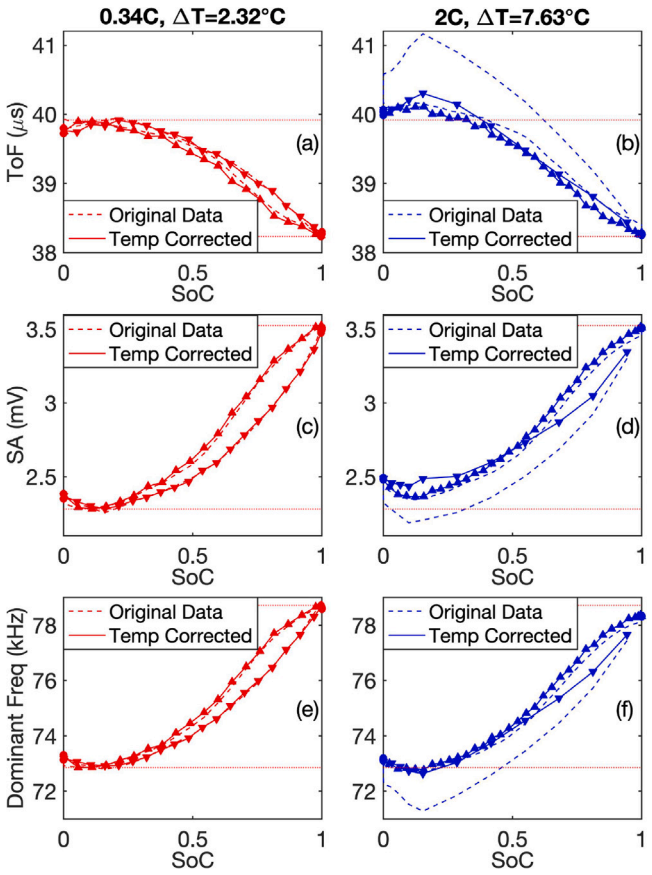

Fig. 6. Original and corrected ToF, SA (second peak) and second dominant frequency for 0.34C cycle recorded on 13.07.2022 (plots a,c,e) and 2C cycle recorded on 14.07.2022 (plots b,d,f) with 1.5 cycle, 65 kHz tone burst reconstructed from 1–600 kHz chirp signal on path 1–2. (For interpretation of the references to colour in this figure legend, the reader is referred to the web version of this article.)

charging; see Section 2.1). Considering the original dominant frequency data shown as the dashed blue line in Fig. 6(f), the low values are striking during discharge, especially at low SoCs. For all cycles, the highest temperature was measured during the discharge at a low SoC, as visualized in Fig. 4(d). Applying the temperature correction model increases the frequency values during discharging significantly, as the original measurements were taken at temperatures up to 32.95 °C. As the cell was left to rest for 30 min after the discharging was completed, the cell temperature during charging was lower, and so is the influence of the temperature correction. Plots 6(b) and (d) show a similar offset using the temperature correction for the ToF and SA.

Thin red lines indicate equal values in each row of plots. In plot (b), the corrected ToF at low charge states is still higher in the $2C$ cycle than in the $0.34C$ cycle (a). For the SA (d) and the dominant frequency (f) recorded during the $2C$ cycle, the ranges of values after applying the temperature correction are close to the respective ranges found for the $0.34C$ cycles in (c) and (e).

3.5. Aging influence

The capacity degradation of Li-ion battery cells is widely discussed for all cell sizes. For portable electronics, it reduces the time the device can be used before it needs to be recharged, whereas for electric vehicles, it leads to a reduced range. The number of cycles to which the cell has been exposed, and correspondingly, the remaining capacity, also influence the parameters which are typically utilized for SoC estimations. Therefore, the aging of cells poses a challenge for the accurate prediction of SoCs [2,4]. The simplest option to measure the remaining capacity is to run a full discharge cycle on the cell and precisely measure the amount of charge that can be drawn from it. This method was used as a reference (ground truth) in this study. However, for batteries built into products it is not feasible to run an entire discharge cycle from 100% to 0% SoC to measure the remaining capacity. It is explored subsequently if ultrasonic guided wave measurements can be used to estimate the cycle age of the cell to supplement the parameters used for SoC prediction algorithm.

The mechanisms which lead to a reduction in capacity are physical changes in the components of the battery cell. The largest impact is due to the growth of the solid electrolyte interface on the carbon anode materials [27]. Thus, the lattice volume of the anode can be increased [27]. Most products use methods such as voltammetry or impedance spectroscopy for remaining capacity estimation which are based on electrochemical measurements. In particular, impedance spectroscopy which is a measurement of cell impedance over a large frequency range, offers a wide range of information. However, this method does not directly measure the physical changes inside the cell, but rather their effect of these changes on the electrochemistry. Therefore, complex models are required to infer physical changes inside the cell [27]. Direct measurements of the changing material properties inside the cell require elaborate methods, such as X-ray diffraction or cell destruction. Hence, these options are not viable for cells in products during operation.

Ultrasonic guided waves change their propagation characteristics based on the material properties. Therefore, not only can changes caused by the variation of SoC and temperature be detected, but also changes in the material properties related to the cell cycle age. Ladpli et al. [10] found a clear trend of a decreasing ToF and increasing SA with the increasing degradation on a 3.65 Ah Li-ion pouch cell. In this section it is explored whether the same trend for the ToF and SA can be found on the larger 12.5 Ah cell used in this study. Furthermore, the impact of the cycle age on the newly introduced dominant frequency is analysed.

The initial 16.41 cycles run on the tested cell (including partial charging and discharging operations) were recorded at various ambient conditions and C-rates. For the aging experiment analysed in this section, 20 additional cycles were recorded. After every fourth $2C$ cycle, one cycle at $0.5C$ was conducted. Because the lifetime of a cell can entail more than a thousand cycles, only small changes could be expected during this experiment.

During the initial four $2C$ cycles of the aging experiment (16.41–20.41 previous cycles), the battery capacity increased, which could be related to incomplete formation at the manufacturer. Starting at 20.41 previous cycles, a clear capacity degradation of approximately 0.02% per cycle was observed. Interestingly, the capacity observed in the $0.5C$ cycles is lower than that of the neighbouring 2C cycles. During the cycles using $2C$ the cell heated up significantly more ($\Delta T = 7.9–12.3$ °C) than during the $0.5C$ cycles ($\Delta T = 1 - 3$ °C). Because the discharging process is diffusion-driven, a higher temperature could enable a larger amount of Li ions to be exchanged between the electrodes, which could explain the increased capacity.

Corresponding to the capacity degradation for the cycles with a previous cycle count of 20.41–35.41, changes in ToF, SA, and dominant frequency are observed. Therefore, guided wave features can be utilized to estimate the remaining capacity. To isolate the signal changes caused by decreasing state-of-health (SoH, normalized remaining capacity), the present SoC must be known. As devices with batteries (phones, notebooks, and cars) are frequently charged to 100% SoC, this state is chosen as an SoC reference to monitor the SoH. The variations in the ToF, SA, and dominant frequency at 100% SoC are shown in Fig. 7.

The empty circles in Fig. 7 indicate the measurements obtained at 100% SoC throughout the aging experiment. It is clear that the scatter, especially for the ToF (a) and dominant frequency (c), is very wide. The filled circles indicate the mean value for each x-station, and the dashed

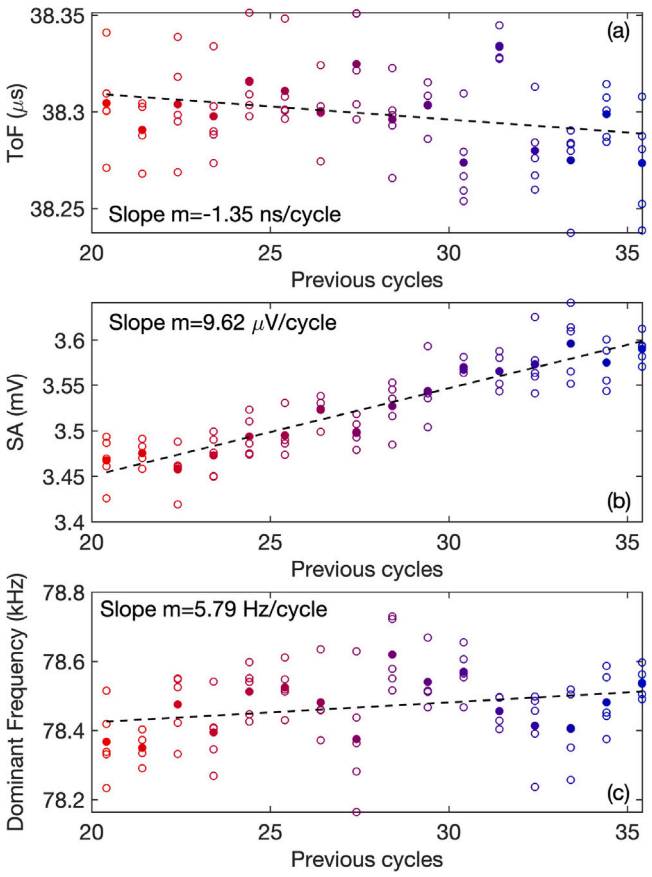

Fig. 7. Datapoints (empty circles), mean value at each x-station (filled circles) and linear regression (dashed black) for ToF (a), SA (b), and dominant frequency (c) at 100% SoC with temperature correction for 1.5 cycle 65 kHz tone burst reconstructed from 1–600 kHz chirp on path 1-2.

black line is the result of a linear regression of the averages. For the SA (b) an increase with the number of cycles can be confirmed. For the dominant frequency (c) and ToF (a), the number of aging cycles is not large enough to establish a robust prediction. To this end, and to check for nonlinear effects which Ladpli et al. [10] found after approximately 125 cycles, multiple cells would need to be cycled for the duration of a cell life.

Nevertheless, as an indication, the slopes of the trendlines are added in the last column of Table 1 comparing them to the SoC and temperature influences on the indicators. From this summary, it becomes clear that neither the influence of temperature nor the influence of aging can be ignored if guided wave features are used to predict the SoC accurately. The temperature variation during one cycle can easily exceed 10 °C, leading to >50% variation in ToF and >25% variation in SA and dominant frequency compared to the range of values found between 0% and 100% SoC. Considering the aging trend for the SA, an error in SoC of 25% would be exceeded after only 33 cycles.

3.6. State-of-charge prediction

Advanced methods are available for predicting SoCs of Li-ion batteries. In addition to simple analytical models, recurrent neural network have been introduced to create multi-parameter-based predictions which can account for variations in voltage, current, temperature, and aging [2,4,15]. These models could be further enhanced by introducing ultrasonic guided-wave signal data. However, this work is focused on the validation of the ultrasonic parameters which could be used as input to these models. Therefore, in this work, a simple model assuming a quadratic correlation between the ultrasonic parameters and SoC is used to compare the prediction performance of the dominant frequency, ToF, and SA on the WS-NCM12.5AH-3.7 battery cell. Furthermore, precision improvements through temperature and aging corrections are discussed. For the prediction models, the cycles recorded in the aging experiment after 20.41–35.41 previous cycles are used.

Fig. 8 presents the regression model for the SoC based on the second dominant frequency. The data points used for the regression (empty circles) have been corrected for the influence of temperature (Section 3.4) and aging (Section 3.5).

To account for the cycle age in any new cycle j, multiple dominant frequency measurements recorded at 100% SoC were averaged and the result denoted as $\overline{f}_{j,SoC=1}$. The first cycle of the series shown in Fig. 7 was chosen as the reference $\overline{f}_{1,SoC=1}$. Subsequently, for the new cycle j the impact of the cell age on the dominant frequency is calculated using Eq. (6) and subtracted from all measurements in this cycle per Eq. (7). This approach assumes that the effect of the cycle age is independent of the SoC, as the same correction $\Delta f_{j,age}$ is used for all charge states.

$$\Delta f_{j,age} = \overline{f}_{j,SoC=1,} - \overline{f}_{1,SoC=1} \tag{6}$$

$$f_{j,SoC=x,corrected} = f_{j,SoC=x} - \Delta f_{j,age} \tag{7}$$

In the previous discussion on the dominant frequency (Fig. 5), it has been identified that $d(f)/d(SoC) \approx 0$ at 0% SoC (similar to ToF and SA). Therefore, it was to be expected that the accuracy of the SoC prediction would be worse for low charge states. Fig. 8 illustrates this result. The root mean squared error (RMSE) and maximum error are shown as dashed and dotted lines, respectively, for each quarter of the dominant frequency range. Whereas the RMSE in the first quarter (lowest SoC) is ±11.51%, it decreases to ±4.41% in the last quarter (highest SoC).

Next, the quality of the temperature and aging correction models is evaluated based on the error of the regression for each ultrasonic indicator. Table 2 compares the accuracy of the prediction model for each quarter of the prediction-parameter range. Even without any correction, the trend of decreasing error with increasing SoC can be read from the first data line of the table. The second data line displays the RMSE for the prediction based on temperature-corrected values. For quarters 1–2, a reduction of 2.37% to 3.66% in the RMSE of the SoC prediction is evident. For the last quarter, in which the error is already the smallest, a slight increase of 0.37% can be observed. As discussed before and shown in Fig. 4, the cell temperature increases during the discharge cycle. Therefore, the temperature variation is the highest for low charge states. For high SoCs, temperature variability is much smaller. The correction introduced for the temperature influence has associated sources of error. Therefore, the already small RMSE at high states of charge cannot be further improved using temperature-corrected values.

The third data line in Table 2 shows the RMSE of the model using temperature and aging corrections. It is clear from the data that aging correction has no major impact on the accuracy of the prediction. This was expected based on the uncertain trend of the dominant frequency with increasing cycle age, shown in Fig. 7. However, if a larger number of cycles (e.g. 200 cycles) would be analysed, age correction might become more relevant for the dominant frequency-based SoC prediction.

A similar regression model was built to estimate the SoC based on the SA. Data rows 4–6 in Table 2 illustrate the RMSE for the prediction model based on the SA. Here, the temperature correction has a smaller impact on the prediction accuracy compared to the dominant frequency-based model. However, as already expected from Fig. 7, the aging correction has a more significant impact with an improvement of up to 1.02% in RMSE compared to the data corrected only for the temperature impact. Considering that only 16 cycles were included in the analysis, the 1.02% deviation is substantial.

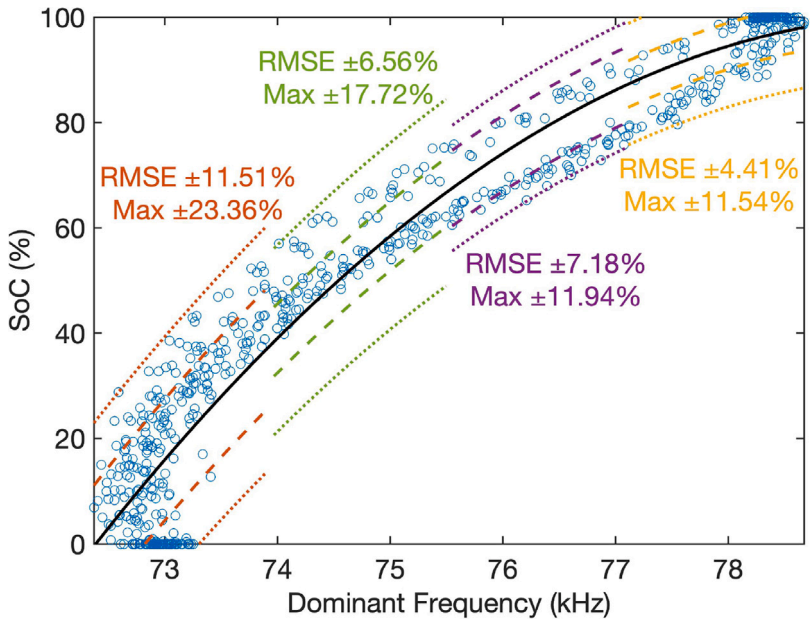

Fig. 8. Second dominant frequency (empty blue circles) with temperature and age correction for 16 cycles (20–35 previous cycles) for path 1–2; Second order regression polynomial (black line); RMSE (dashed lines) and maximum error (dotted lines). (For interpretation of the references to colour in this figure legend, the reader is referred to the web version of this article.)

Table 2
RMSE error for SoC prediction.

Prediction basis	Data correction	1. Quarter (lowest SoC)	2. Quarter	3. Quarter	4. Quarter (highest SoC)	Global
Dominant frequency	Original	13.85%	10.29%	7.09%	4.04%	10.01%
	Temperature	11.47%	6.63%	7.09%	4.42%	8.73%
	Temperature & cycle age	11.51%	6.56%	7.18%	4.41%	8.76%
Signal amplitude	Original	14.44%	13.64%	7.29%	3.80%	11.38%
	Temperature	16.05%	10.12%	6.11%	3.74%	11.81%
	Temperature & cycle age	15.02%	9.91%	6.23%	3.26%	11.11%
Time of flight	Original	18.70%	14.01%	9.51%	2.98%	11.34%
	Temperature	11.77%	5.97%	5.11%	3.72%	8.48%
	Temperature & cycle age	11.89%	5.90%	4.99%	3.70%	8.55%

The SoC prediction based on ToF displays similar trends to the dominant frequency-based prediction. The corresponding error comparison is summarized in the last three rows of Table 2.

The last column of Table 2 presents the RMSE for the entire SoC range. The model using ToF achieves 8.55% RMSE, outperforming the model using SA (11.11% RMSE). Predicting the SoC based on the dominant frequency results in an RMSE of 8.76%. Because three indicators were available, an additional model was created using a combination of them. A second-order polynomial without cross-terms, as shown in Eq. (8) was used to lower the RMSE of the SoC estimate by 0.91% to 7.64% compared with the ToF-based model. If a second-order multivariable model including cross-terms is employed, an RMSE of 7.59% can be achieved, resulting in an improvement of only 0.05% compared to the model shown in Eq. (8).

$$SoC = m_0 + m_{11}(ToF) + m_{12}(ToF)^2 + m_{21}SA + m_{22}(SA)^2 + m_{31}f + m_{32}f^2 \quad (8)$$

To put the obtained RMSE values into context, a comparison with the SoC prediction models of Liu et al. [15] and Wang et al. [2] shall be drawn. They achieved average RMSE of 3.757% and 3.53%, respectively, using different types of neural networks. While such algorithms can capture nonlinear trends and multivariable dependencies easily, they have the disadvantage that the prediction is not physics-based. Therefore, the causes and consequences of variations in the ambient conditions or cell parameters cannot be retrieved. For example, Liu et al. [15] used only data recorded during charging and discharging with $1C$ to train the network. However, in this study, it is found that the C-rate influences guided wave propagation through temperature variations and potentially through other effects. To make a neural network robust to such variations, a large amount of data is required. The network must be trained with data collected under different conditions because small changes in the input can lead to large errors in the predictive output of a neural network.

4. Conclusion

This study proposes a novel method of using chirp signals to optimize Hanning-windowed ultrasound tone burst signals for probing the SoC, SoH, and temperature of battery pouch cells. The wave packets in the response signal are more confined using a small number of cycles in the excitation signal. The frequency of the excitation signal can be optimized without prior knowledge of the cell architecture, to account for the different sizes, constituents, and stacking of different cells. The dominant frequency of the response to a Hanning-windowed tone burst signal is analysed with fine frequency resolution to enable its use as an SoC indicator. Compared to the ToF and SA of ultrasonic guided waves, which were used in earlier research [8,10], the dominant frequency offers almost the same predictive accuracy while being less sensitive to temperature changes. However, it is computationally more expensive because it requires a high-fidelity discrete Fourier transform to obtain the dominant frequency with sufficient resolution. The developed prediction algorithm for the SoC confirms the performance of the dominant

frequency-based model. Furthermore, it shows that the ToF and SA may be used to indicate the SoC not only for small cells, as shown in previous studies [8,10,15], but also for cells with capacities suitable for electric vehicles. Moreover, the study identifies that both temperature and cycle age have a significant impact on all the considered indicators. Each error was isolated to produce a clear correlation between the SoC and the wave features.

Two domains of further research appear interesting: First, the existing correlations should be further refined to produce more reliable and precise SoC predictions. The prediction in the low SoC region may be enhanced by adding the derivatives of the indicators $\partial(ToF)/\partial(SoC)$, $\partial(SA)/\partial(SoC)$, and $\partial(f)/\partial(SoC)$ as parameters for the model. In addition, the cell voltage and current are easy to obtain and already used in battery management systems. Especially for low states of charge, the cell voltage shows a large variation which complements the guided wave-based prediction well. Combining the electrical parameters and guided-wave-based indicators might enable the development of an algorithm to predict the SoC, SoH, and temperature simultaneously with great accuracy.

The second field of interest is the identification of abnormal situations. Appleberry et al. [28] developed an early thermal runaway (battery fire) warning mechanism for selected failure mechanisms on a small Li-ion battery using conventional ultrasonic transducers. If a similar warning mechanism can be developed using ultrasonic guided waves with small disc transducers, it could be integrated into real-world products. In addition to thermal runaway, it might be possible to identify other failure mechanisms. Excessive self-discharge could not only be identified through the SoC but also by identifying the material changes leading to self-discharge in the first place.

CRediT authorship contribution statement

Benjamin Reichmann: Conceptualization, Methodology, Experiments, Data analysis, Writing – original draft. **Zahra Sharif-Khodaei:** Supervision, Resources, Writing – review & editing.

Declaration of competing interest

The authors declare the following financial interests/personal relationships which may be considered as potential competing interests: Zahra Sharif Khodaei reports financial support was provided by Imperial College London. Zahra Sharif Khodaei reports a relationship with Imperial College London that includes: employment.

Data availability

Data will be made available on request.

References

[1] L. Paoli, T. Guel, Electric cars fend off supply challenges to more than double global sales – analysis, 2022, URL: https://www.iea.org/commentaries/electric-cars-fend-off-supply-challenges-to-more-than-double-global-sales (accessed on 23.08.2022).
[2] S. Wang, P. Takyi-Aninakwa, S. Jin, C. Yu, C. Fernandez, D.-I. Stroe, An improved feedforward-long short-term memory modeling method for the whole-life-cycle state of charge prediction of lithium-ion batteries considering current-voltage-temperature variation, Energy 254 (2022) 124224.
[3] S. Wang, P. Ren, P. Takyi-Aninakwa, S. Jin, C. Fernandez, A critical review of improved deep convolutional neural network for multi-timescale state prediction of lithium-ion batteries, Energies 15 (14) (2022) 5053.
[4] S. Wang, Y. Fan, S. Jin, P. Takyi-Aninakwa, C. Fernandez, Improved anti-noise adaptive long short-term memory neural network modeling for the robust remaining useful life prediction of lithium-ion batteries, Reliab. Eng. Syst. Saf. 230 (2023) 108920.
[5] M.F. Aliabadi, Z.S. Khodaei, Structural Health Monitoring for Advanced Composite Structures, Vol. 8, World Scientific, 2017.
[6] I. Dafydd, Z. Sharif Khodaei, Analysis of barely visible impact damage severity with ultrasonic guided Lamb waves, Struct. Health Monit. 19 (4) (2020) 1104–1122.
[7] N. Yue, Z.S. Khodaei, M. Aliabadi, Damage detection in large composite stiffened panels based on a novel SHM building block philosophy, Smart Mater. Struct. 30 (4) (2021) 045004.
[8] L. Gold, T. Bach, W. Virsik, A. Schmitt, J. Müller, T.E. Staab, G. Sextl, Probing lithium-ion batteries' state-of-charge using ultrasonic transmission–Concept and laboratory testing, J. Power Sources 343 (2017) 536–544.
[9] A. Hsieh, S. Bhadra, B. Hertzberg, P. Gjeltema, A. Goy, J.W. Fleischer, D.A. Steingart, Electrochemical-acoustic time of flight: in operando correlation of physical dynamics with battery charge and health, Energy Environ. Sci. 8 (5) (2015) 1569–1577.
[10] P. Ladpli, F. Kopsaftopoulos, F.-K. Chang, Estimating state of charge and health of lithium-ion batteries with guided waves using built-in piezoelectric sensors/actuators, J. Power Sources 384 (2018) 342–354.
[11] Z. Deng, X. Lin, Z. Huang, J. Meng, Y. Zhong, G. Ma, Y. Zhou, Y. Shen, H. Ding, Y. Huang, Recent progress on advanced imaging techniques for lithium-ion batteries, Adv. Energy Mater. 11 (2) (2021) 2000806.
[12] B. Sood, M. Osterman, M. Pecht, Health monitoring of lithium-ion batteries, in: 2013 IEEE Symposium on Product Compliance Engineering (ISPCE), IEEE, 2013, pp. 1–6.
[13] J.B. Robinson, M. Maier, G. Alster, T. Compton, D.J. Brett, P.R. Shearing, Spatially resolved ultrasound diagnostics of Li-ion battery electrodes, Phys. Chem. Chem. Phys. 21 (12) (2019) 6354–6361.
[14] R.E. Owen, J.B. Robinson, J.S. Weaving, M.T. Pham, T.G. Tranter, T.P. Neville, D. Billson, M. Braglia, R. Stocker, A.A. Tidblad, et al., Operando ultrasonic monitoring of lithium-ion battery temperature and behaviour at different cycling rates and under drive cycle conditions, J. Electrochem. Soc. 169 (4) (2022) 040563.
[15] Y. Liu, R. Zhang, W. Hao, Evaluation of the state of charge of lithium-ion batteries using ultrasonic guided waves and artificial neural network, Ionics (2022) 1–12.
[16] Z. Su, L. Ye, Identification of Damage using Lamb Waves: From Fundamentals To Applications, Vol. 48, Springer Science & Business Media, 2009.
[17] J.T. Warner, The Handbook of Lithium-Ion Battery Pack Design: Chemistry, Components, Types and Terminology, Elsevier, 2015.
[18] F. Lambinet, Z. Sharif Khodaei, Measurement platform for structural health monitoring application of large scale structures, Measurement 190 (2022) 110675.
[19] F. De Sá Rodrigues, A. Hami-Seno, Z. Sharif-Khodaei, M. Aliabadi, Structural Health Monitoring platform for industrial scale composite structures, in: AIP Conference Proceedings, Vol. XXX, AIP Publishing LLC, 2023, 020008.
[20] Z. Sharif-Khodaei, M. Aliabadi, Assessment of delay-and-sum algorithms for damage detection in aluminium and composite plates, Smart Mater. Struct. 23 (7) (2014) 075007.
[21] J.E. Michaels, S.J. Lee, A.J. Croxford, P.D. Wilcox, Chirp excitation of ultrasonic guided waves, Ultrasonics 53 (1) (2013) 265–270.
[22] I. Dafydd, Z.S. Khodaei, Damage severity assessment in composite structures using ultrasonic guided waves with chirp excitation, in: Sensors and Smart Structures Technologies for Civil, Mechanical, and Aerospace Systems 2018, Vol. 10598, SPIE, 2018, pp. 83–93.
[23] M. Salmanpour, Z. Sharif Khodaei, M. Aliabadi, Guided wave temperature correction methods in structural health monitoring, J. Intell. Mater. Syst. Struct. 28 (5) (2017) 604–618.
[24] D. Perfetto, Z.S. Khodaei, A. De Luca, M. Aliabadi, F. Caputo, Experiments and modelling of ultrasonic waves in composite plates under varying temperature, Ultrasonics 126 (2022) 106820.
[25] I.N. Giannakeas, Z. Sharif Khodaei, M. Aliabadi, An up-scaling temperature compensation framework for guided wave–based structural health monitoring in large composite structures, Struct. Health Monit. (2022) 14759217221095415.
[26] N. Yue, M. Aliabadi, A scalable data-driven approach to temperature baseline reconstruction for guided wave structural health monitoring of anisotropic carbon-fibre-reinforced polymer structures, Struct. Health Monit. 19 (5) (2020) 1487–1506.
[27] U. Tröltzsch, O. Kanoun, H.-R. Tränkler, Characterizing aging effects of lithium ion batteries by impedance spectroscopy, Electrochim. Acta 51 (8–9) (2006) 1664–1672.
[28] M.C. Appleberry, J.A. Kowalski, S.A. Africk, J. Mitchell, T.C. Ferree, V. Chang, V. Parekh, Z. Xu, Z. Ye, J.F. Whitacre, et al., Avoiding thermal runaway in lithium-ion batteries using ultrasound detection of early failure mechanisms, J. Power Sources 535 (2022) 231423.